Bulletin of Engineering Geology and the Environment (2026) 85:426
https://doi.org/10.1007/s10064-026-05104-w

ORIGINAL PAPER

Analysis of the May 2019 Joffre Peak landslides, British Columbia, Canada: The importance of considering changes in slope kinematics

Nicola Fullin[1,2] · Davide Donati[3] · Doug Stead[4] · Lisa Borgatti[3] · Monica Ghirotti[1]

Received: 10 November 2025 / Accepted: 20 June 2026
© The Author(s) 2026

Abstract

This work presents a workflow to investigate the evolution of slope kinematics during the detachment of multi-stage rockslides, using the 2019 Joffre Peak landslide (Canada) as a case study. The Joffre Peak failure developed through multiple temporally and kinematically connected stages, in which successive events progressively modified slope geometry, boundary conditions, and failure mechanisms. Particular attention is devoted to reconstructing how slope morphology and kinematics evolved throughout the different failure stages. The proposed approach combines remote sensing, structural analysis, and discontinuous numerical modelling, supported by high-resolution point clouds for multi-scale characterization of the rock slope. At the slope scale, three main lineament trends were identified through GIS-based analysis, while at the outcrop scale seven discontinuity sets were characterized using a window-mapping technique. Results indicate that high-persistence discontinuities controlled the rear and lateral release surfaces of the landslide blocks, whereas the basal sliding surface, buried beneath debris deposits, can only be constrained through multi-temporal kinematic reconstruction. Two kinematic scenarios are proposed to explain landslide evolution. The first involves sliding along a slope-dipping discontinuity, whereas the second suggests that the later failure stage evolved toward a wedge-sliding mechanism induced by progressive geometrical changes after the initial collapse. Discontinuous 3D numerical modelling demonstrates that both scenarios are kinematically feasible and highlights the strong structural and mechanical interaction between successive landslide stages. Although a unique failure mechanism cannot be conclusively identified, the study demonstrates that accounting for evolving slope kinematics is essential for reliable geomorphic interpretation and rock slope stability assessment in multi-stage landslides.

Keywords Slope kinematics · Remote sensing · Numerical modelling · Multi-stage landslides

Introduction

Landslides are a major natural hazard that result in thousands of casualties each year (Froude and Petley 2018). These events can be triggered by rainfall (Crosta and Frattini 2003; Iverson 2000), earthquakes (Bozzano et al. 2011; Keefer 2002), anthropogenic activities (Cascini et al. 2008; Michoud et al. 2012; Laimer 2017; Jaboyedoff et al. 2018), as well as progressive damage (Donati et al. 2021, 2023). At higher elevations and latitudes, permafrost degradation (e.g., Fischer et al. 2006; Gruber and Haeberli 2007), glacial retreat (e.g., Fischer et al. 2012; Kos et al. 2016; Donati et al. 2022; Lemaire et al. 2024), and subsequent decrease in lateral support at the toe (e.g., McColl 2012; Grämiger et al. 2017) can also contribute to instability phenomena, inducing slope instabilities that may vary significantly in terms of velocity and extent (Hungr 2007; Legros 2002). Despite the

✉ Davide Donati
davide.donati17@unibo.it

1 Department of Physics and Earth Sciences, University of Ferrara, Ferrara 44122, Italy

2 Italian National Research Council (CNR), Research Institute for Geo-Hydrological Protection (IRPI), Corso Stati Uniti 4, Padova 35127, Italy

3 Department of Civil, Chemical, Environmental, and Materials Engineering, Alma Mater Studiorum - University of Bologna, Bologna 40126, Italy

4 Department of Earth Sciences, Simon Fraser University, Burnaby, British, Columbia V5A 1S6, Canada

Published online: 26 June 2026

recognized importance and harmful impacts of these natural events, and due to the intrinsic challenges that characterize geological data collection, the investigation of landslides is affected by significant uncertainties. To date, the interpretation of geological and environmental processes, geomorphic evolution, controlling factors, and post-failure behavior of landslides remains a particularly challenging task (Stead and Eberhardt 2013; Lacroix et al. 2020). As a result, a complete understanding of the evolution of landslides, and hence the ability to comprehensively characterize, describe, and ultimately forecast the failure of landslide events is limited to only a relatively small number of cases (Mazzanti et al. 2015; Manconi and Giordan 2016; Sättele et al. 2016; Carlà et al. 2017, 2019; Leinauer et al. 2023; Loew et al. 2025). Additionally, forecasting rock slope failure, relying predominantly on displacement monitoring data and trend evaluations, remains extremely challenging where instability is controlled by brittle fracturing of intact material (Rose and Hungr 2007; Mufundirwa et al. 2010).

In most cases, rock slope deformation and landslide displacement are controlled by discrete or persistent structures that can affect the geological material at the scale of intact rock (mm or sub-mm scale, e.g., micro-cracks and intact rock flaws, foliation), rock mass (cm to m scale, e.g., joints, fractures, bedding, faults), and rock slope (tens to hundreds of m, e.g., regional faults and folds, shear zones). These features can provide basal, rear, and lateral release of landslides at all scales (Brideau et al. 2009; Stead and Wolter 2015). Therefore, the correct identification of geological structures and their geometrical relation with the slope morphology is of paramount importance for inferring the behavior and stability of rock slopes in both the short and long term. Structural discontinuities can also propagate through progressive brittle fracturing of intact rock, further reducing kinematic constraints and providing kinematic freedom to volumes of previously stable rock masses (Donati et al. 2021; He et al. 2022). Kinematic freedom has been defined as the capability of a discrete, removable (e.g., physically separated by discontinuities) volume in a rock slope to displace due to gravitational force (Donati et al. 2023). In some cases, the combined effects of these factors can promote the development of multi-stage landslides. For the purpose of this work, multi-stage landslides are represented by a series of events in which one or more blocks detach as a consequence of a previous slope instability event. This may be due to instability-induced changes in stress distribution and/or in slope kinematics (regardless of the time span between failure events). Donati et al. (2021) investigated the multi-stage nature of the Hope Slide (BC, Canada) showing that both stress redistribution and progressive damage accumulation caused by a prehistoric failure eventually led to a destructive event in 1965, which occurred in multiple stages itself. Other examples of multi-stage rockslides include the Randa rockslides (Sartori et al. 2003; Willenberg et al. 2008), the Palliser rockslide (Sturzenegger et al. 2015), the Preonzo rock slope failure (Gschwind et al. 2019) and the Elliot Creek landslide (Geertsema et al. 2022). However, due to their relatively low frequency, few multi-stage landslides have been directly witnessed (Bromhead et al. 1996; Brideau et al. 2009) and sufficiently large databases to allow a comprehensive characterization and interpretation of the phenomenon are seldom available.

The collection of structural and geomechanical data in the field can be challenging, due to hazardous conditions posed by post-event and residual activity of the slope (e.g., rock fall) and the presence of overhanging or unstable blocks. The same challenges can also limit or prevent the identification of incipient re-activation, enlargement, retrogression, or secondary instability development that are typical of multi-stage events. Significant progress has been made over the past two decades in the collection of geostructural information using remote sensing techniques (e.g., Jaboyedoff et al. 2012; Casagli et al. 2017; Vanneschi et al. 2017; Stead et al. 2019; Salvini et al. 2020; Perozzo et al. 2024). Three-dimensional point clouds obtained from airborne and terrestrial laser scanning (Jaboyedoff et al. 2012) or digital photogrammetric methods, such as Structure-from-Motion (SfM, Westoby et al. 2012; Bar et al. 2021) are today routinely employed to perform discontinuity mapping and geomechanical rock mass characterization. High-resolution topographic data obtained through remote sensing techniques can also be used as input data for numerical modeling simulations (Francioni et al. 2018a, b). The combined use of remote sensing and numerical modelling is now widespread as successfully demonstrated by a vast literature (Corkum and Martin 2004; Firpo et al. 2011; Scholtès and Donzé 2012; Havaej et al. 2016; Spreafico et al. 2016; Carlà et al. 2024). In particular, the distinct element method (DEM) is useful in modelling the deformation and failure of structurally controlled rock slope instabilities. DEM is a numerical modeling technique capable of simulating the displacement, rotation, and detachment of independent blocks along discrete discontinuities (Cundall 1988), as well as the progressive evolution of the instability process with time (Brideau et al. 2011). DEM is especially effective in analyzing multi-stage landslides (Gerstner et al. 2023), as the displacement and detachment of independent blocks at different times can be simulated within the same model run.

In this paper, the role of the geomorphic evolution of rock slopes due to multi-stage landslides is investigated in combination with the importance of subsequent changes in slope kinematics. In particular, it is emphasized that slope kinematic analysis performed with different slope configurations can allow the evolution of the failure mechanisms of

different landslide events to be captured. To do so, we use a workflow combining remote sensing surveys and numerical modeling analyses to investigate the Joffre Peak landslide, a multi-stage landslide event that occurred in 2019 in British Columbia (Canada). First, discontinuity mapping and rock mass characterization using a SfM-derived 3D model are performed. The results of the discontinuity mapping, combined with the reconstructed pre- and post-failure slope geometry, are used to conduct a 3D numerical analysis of the failures, aimed at highlighting the kinematic relationship between the two blocks that detached during the 2019 landslide events. In particular, two scenarios, which differ in the morphology of the basal surface (not visible in the field due to the presence of a talus deposit), are investigated and discussed, in order to explain the multi-stage nature of the landslide. The critical role that slope kinematics played in controlling the Joffre Peak landslides is emphasized, demonstrating that multi-temporal kinematic analyses can be crucial in the development and assessment of failure scenarios. Ultimately, the study shows that the proposed approach can be a critical tool in the characterization of multi-stage landslide failure mechanisms in rock slopes.

Overview of the study site

Joffre Peak is located in southern British Columbia (Fig. 1), along the Coast Mountain Belt (western Canada), about 130 km north of Vancouver and 20 km east of Pemberton. The Joffre Peak reaches an elevation of 2721 m a.s.l. (above sea level) and is the second highest peak of the Joffre Group (after Mount Matier, 2783 m a.s.l.). Joffre Peak is the highest point in a 3-km-long, NW-SE-oriented mountain ridge that extends from Mount Matier (to the south) to Cayoosh Creek (to the north).

The Joffre slope instability process can be preliminarily described as a multi-stage rock planar slide-ice/rock avalanche (Hungr et al. 2014) displaying a complex style of activity. In May 2019, two large landslides detached from the northern slope of the Joffre Peak (Fig. 1). The first landslide occurred on May 13th at 7:40 am (as evident from seismic signals, Friele et al. 2020) and formed a 180 m high, 130 m wide scar on the side of the rock slope (Fig. 2). The landslide travelled for about 4 km within the valley below, referred to as Cerise Creek. The second landslide detached at 9:03 a.m. on May 16th and involved an adjacent rock mass block located south of the scar of the first landslide. The second event extended the width of the fresh scar by 180 m. The landslide material traveled almost 6 km along the Cerise Creek, stopping 300 m before crossing Highway 99, progressively evolving from a rock avalanche to a debris flow and eventually a debris flood (Friele et al. 2020).

The slope from which the landslides detached is a 250 m-high, NE dipping, sub-vertical cliff. The landslide scarp is formed by very high persistence (according to ISRM, 1978) geological structures. A major, sub-vertical NW-SE trending structure, sub-parallel to the original slope, appears to form the rear release surface of both failure events, whereas the lateral release surfaces are formed by sub-vertical, NE-SW trending structures. While the location of the rear and lateral release surfaces is clear, assessing the persistence and the orientation of the basal sliding surface is considerably more challenging, as it is completely covered by debris.

The bedrock forming the Joffre Peak area consists of diorite, granodiorite and quartz-diorite which are part of a Cretaceous pluton that intruded the intermontane domain Cadwallader Group (Fig. 3; Vandall 1993) and is overlain by arc-related volcanic and sedimentary rocks (Bustin et al. 2013). From a tectonic perspective, the ridge that comprises Joffre Peak is located in the hanging wall of a high angle, compressional, SW dipping fault, referred to as the Owl Creek Fault (Fig. 3), which brings into contact sedimentary deposits of the Gambier Group and plutonic

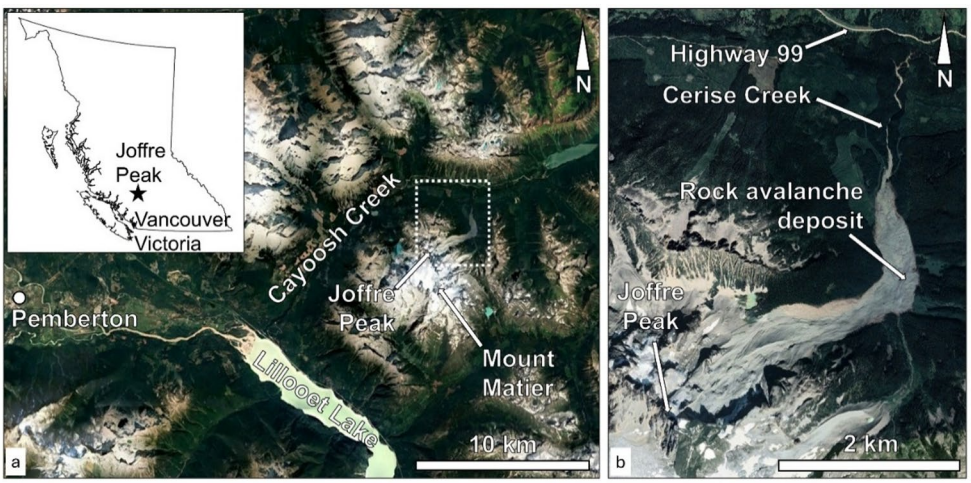


Fig. 1 Satellite imagery of the investigated region (Maxar Technologies, from Google Earth). a: location of Joffre Peak in the section of Coast Belt Mountain near Pemberton (BC, Canada). In the inset, the location of Joffre Peak in British Columbia is shown. b: view of the landslide deposit along Cerise Creek and the area affected by the landslides

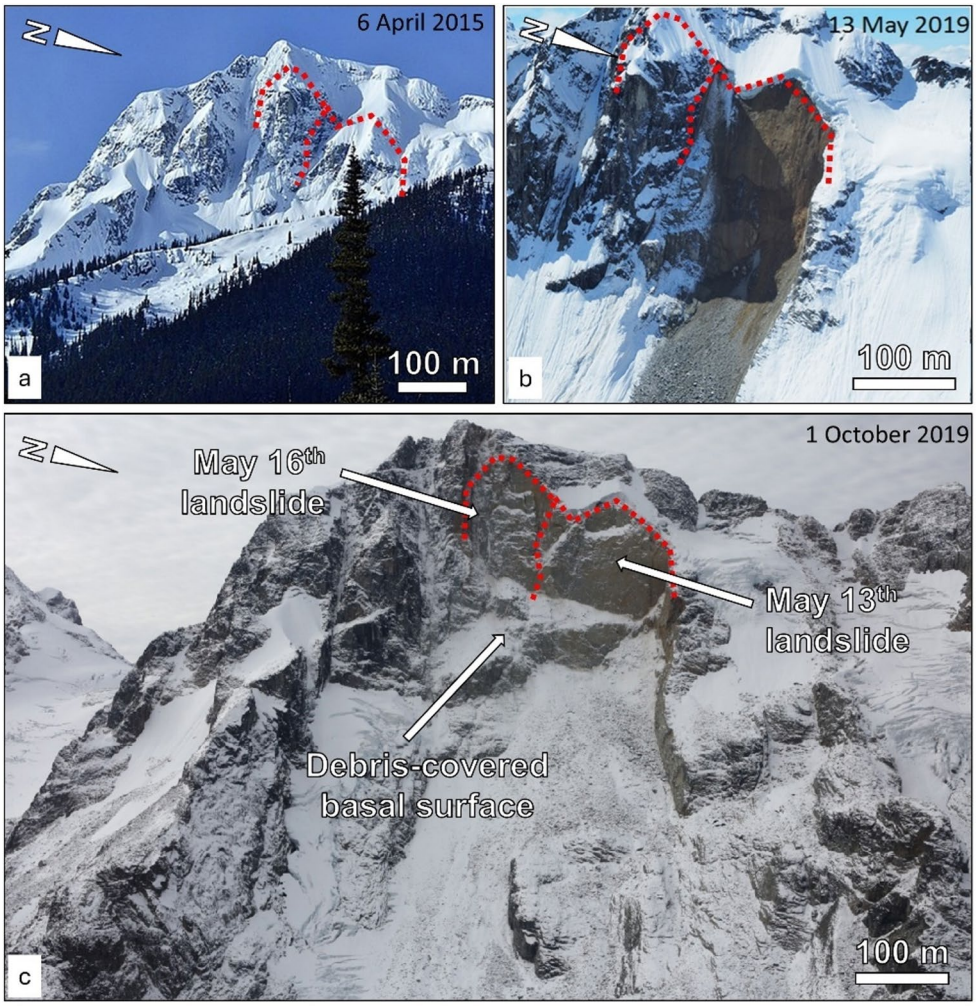


Fig. 2 Summary of the evolution of the Joffre Peak, showing the inferred extent of the landslides. **a**: View of the Joffre Peak prior to the landslides, taken from Highway 99 (2015 photograph by Pan Shibo, via Wikimedia Commons, CC BY 2.0). **b**: View of Joffre peak on May 13th, 2019, after the first landslide. Note the sub-vertical rear and lateral release surfaces (photograph from Geertsema and Bevington, 2020). **c**: Photograph taken in 2020 showing the post-failure condition of the eastern slope of the Joffre Peak

rocks of the Cadwaller unit (Monger et al. 1982; Bustin et al. 2013; Monger and Gibson 2019).

Methodology

To investigate the Joffre Peak landslides and the role of changes in kinematics on slope instability, a four-step workflow has been developed (Fig. 4). First, aerial photographs from the British Columbia database have been gathered and a helicopter photographic survey of the peak undertaken. Using these datasets, pre- and post-failure 3D models of the slope using a SfM approach have been built. These models have then been used to perform a geomechanical characterization of the rock mass at various scales, and the resulting data post-processed to derive two realistic failure scenarios and the input data for 3D DEM numerical modeling analyses. This procedure will be described in more detail below.

Data collection

Initially, four air photographs taken on July 14th, 2017 (Table 1) were obtained from the BC aerial imagery database (https://www2.gov.bc.ca/gov/content/data/geographic-data-services/digital-imagery/air-photos). All photographs were collected using a Vexcel UltraCam Eagle camera, equipped with a $f = 80$ mm focal length lens, featuring a 261 MegaPixel resolution, a sensor size of and a sensor pixel size of 5.2×5.2 µm. For each air photograph, georeferencing metadata and camera calibration parameters were also obtained. Then, 651 photographs were captured during a helicopter survey conducted on October 2nd, 2019 using a 50 Megapixel Canon EOS 5Ds-R camera and an $f = 50$ mm focal length lens with a Canon GP-E2 GPS receiver mounted externally to geotag the photographs. Photographs were collected at varying distances and directions from the landslide scarp, along all sides of the Joffre Peak. The number of photographs provided redundancy, and the survey aimed at maintaining an overlap in excess of 70% both vertically and laterally for consecutive photographs. Throughout the

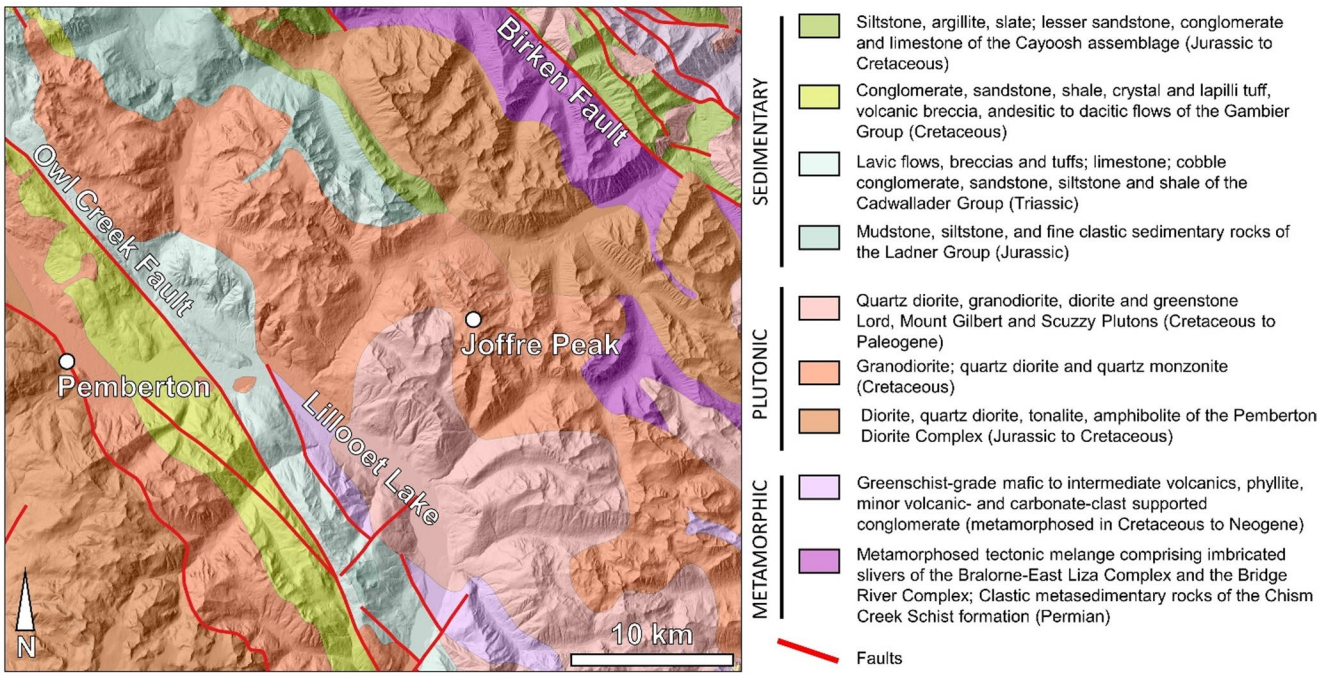


Fig. 3 Geological map of the investigated area (digital data are from Cui et al. 2017; the basemap is a Digital Terrain Model hillshade map from Natural Resource Canada)

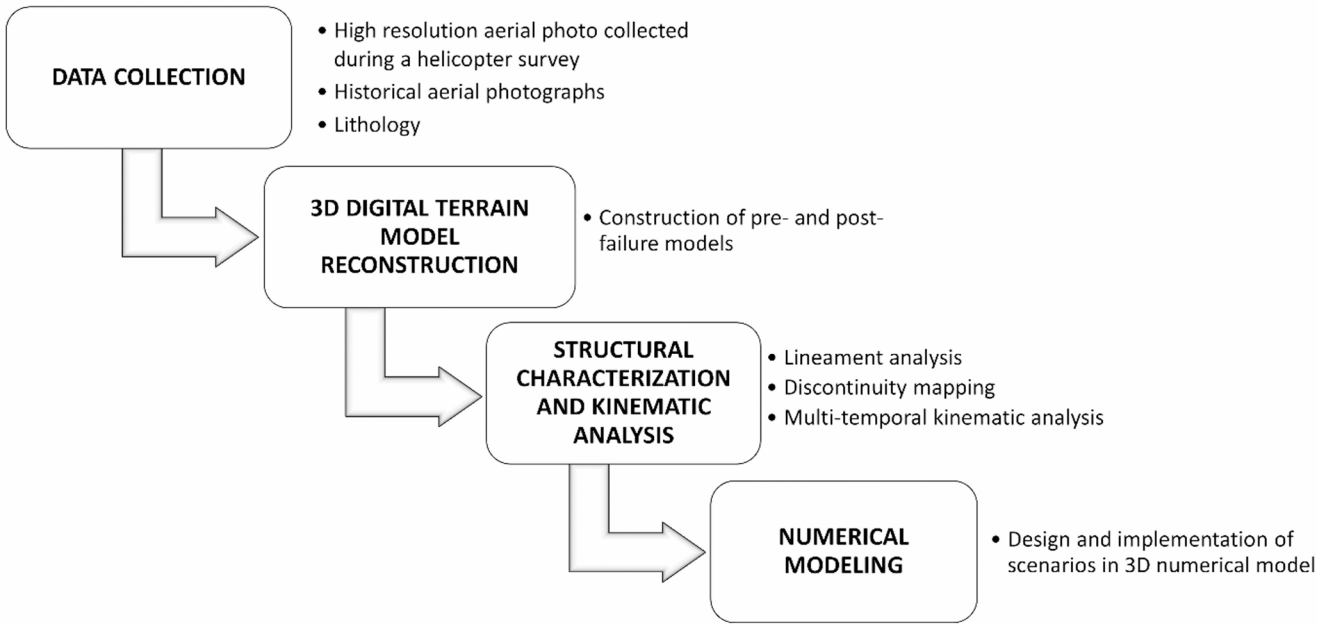


Fig. 4 Workflow of the investigation and analyses undertaken

Table 1 Information on the aerial photographs used to build the pre-failure slope model. Coordinate data indicates the position of the camera (standard deviation, in brackets, indicate accuracy of camera positioning). In all cases, the coordinate system is NAD83/UTM zone 10 N (EPSG: 26910)

Roll - frame	Easting (m)	Northing (m)	Elevation (m)	Scale
bcd17303–802	537884.108 (0.004)	5577255.237 (0.004)	5444.113 (0.005)	1:20000
bcd17303–803	538861.741 (0.004)	5577240.209 (0.004)	5449.392 (0.005)	1:20000
bcd17303–804	539839.662 (0.004)	5577228.673 (0.004)	5460.869 (0.005)	1:20000
bcd17303–805	540817.804 (0.004)	5577227.898 (0.004)	5471.803 (0.005)	1:20000

flight, the distance from the slope ranged between 250 and 500 m.

3D digital terrain model reconstruction

Two different 3D digital terrain models (DTMs) of Joffre Peak, a post-landslide model and a pre-landslide model, were created. The pre-landslide model was built by processing 2017 air photographs. Through a SfM reconstruction in Metashape (Agisoft LCC, 2022) a pre-failure point cloud of the slope was obtained, which was then sub-sampled and meshed using the open-source software Meshlab (Cignoni et al. 2008), to be used as input geometry for the 3D numerical modeling analysis. Sub-sampling was useful to avoid the presence of unnecessarily small elements at the surface of the 3D numerical model, potentially resulting in excessive model surface complexity and model runtime.

The post-landslide model was built in Metashape using the high-resolution digital photographs collected during the helicopter survey. The post-failure point cloud is constituted by 482 million points and is characterized by an average point spacing of 10 cm. The point cloud allowed for both discontinuity mapping and the creation of a post-failure DTM for slope-scale geostructural characterization.

As access to the survey area was prohibited due to safety concerns, it was not possible to position and survey ground control points for the SfM reconstruction or collect rock mass structural measurements directly in the field. Therefore, the pre- and post-failure models were georeferenced solely using the camera position coordinates provided in the metadata (for the historical air photographs) and by the GPS tracker attached to the EOS 5Ds-R camera. The point clouds were then finely registered in the open-source code CloudCompare (CloudCompare 2022) using the pre-failure cloud as reference model. The orientation, scale, and position of the models were then qualitatively evaluated by importing the rasterized elevation datasets into ArcGIS (Esri 2021) and comparing the position and orientation of natural features (scarps, peaks, ridges) with existing basemaps, showing limited angular error in the order of ±2°.

Structural characterization

Geostructural characterization of the slope was performed using a multi-scale approach. First, a slope-scale topographic lineament mapping was performed in ArcGIS, using thematic maps (i.e., hillshade, slope, aspect) derived from the DTM through built-in ArcGIS tools. These maps allowed local variations in slope morphology, which often represent the surface expression of structural geological features, to be identified and mapped as lineaments in the GIS environment. The bearing and length of mapped lineaments were automatically computed also using standard ArcGIS tools. Lineament data were then exported in table format, and their orientation plotted in Rosette diagrams using Dips (RocScience 2024) allowing the major lineament trends to be identified.

Discontinuity mapping was then undertaken at different scales on the post-failure 3D point cloud using CloudCompare. A 50-m arbitrary threshold was assumed to distinguish hierarchically, at this site, 1 st and 2nd order discontinuities, based on the trace length. Initially, 1 st order discontinuities were mapped across the whole post-failure 3D model of the slope (i.e., slope-scale mapping; Fig. 5). Then, 2nd order discontinuities were systematically mapped using a window mapping approach (i.e., window-scale mapping) within two square areas (150 m x 150 m) located on the SW and the SE slopes of the Joffre Peak; these are referred to as Window 1 and Window 2, respectively (Fig. 5). The features mapped at different scales were initially analyzed separately and then compared with each other, and with the slope-scale lineaments. Discontinuity traces longer than 50 m were removed from the window-scale results, in order to avoid redundant data being considered in the analysis.

Discontinuity orientation data were used to perform kinematic analysis using the software Dips. The orientation of discontinuity traces and planes mapped at the slope and window scales were analyzed and compared, in order to identify the main discontinuity sets within the rock mass. Kinematic analysis was performed to identify the potential failure mechanisms controlling the two landslide events.

The original Joffre Peak slope orientation was initially considered to investigate at multiple scales the role of discontinuities on the detachment of the first landslide. Then, to account for the changes in morphology, kinematic conditions and constraints, the new slope orientation resulting from the detachment of the first landslide was also considered by graphically extending the instability envelopes on the stereonets. Using this approach, the potential changes in failure mechanisms involved in the multi-stage landslide were investigated, and their effects on the stability and behavior of the landslide blocks illustrated. This approach is important in order to identify the role that the first event may have played in kinematically controlling the second event, for example by acting as a key block within the original rock slope (Goodman 1995).

Numerical modeling

The numerical analysis was undertaken using the 3D numerical modelling code 3DEC (Itasca 2021a, b), which allows for the analysis of structurally controlled slope failures (Cundall 1988). The pre-failure 3D model was imported into the 3D CAD software Rhinoceros 6 (McNeel

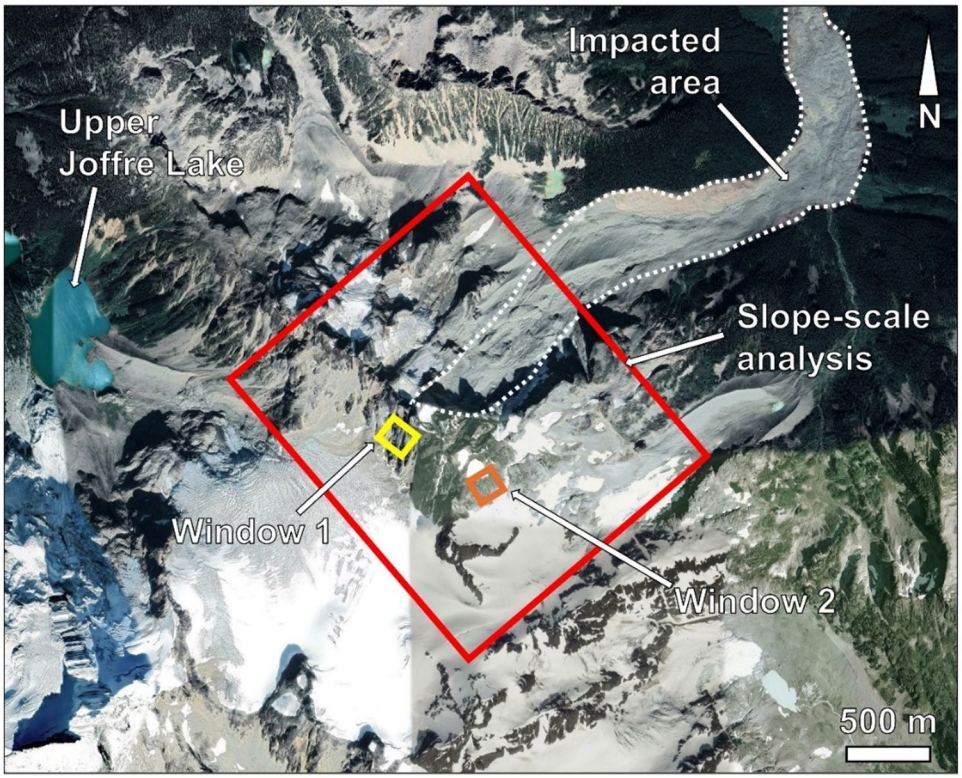


Fig. 5 Overview of the area where structural analyses were performed. Red square shows the extent of the slope scale (i.e., 1 st order) discontinuity mapping area. Yellow and orange squares outline the approximate locations window 1 and window 2, respectively, where 2nd order discontinuity mapping was conducted (satellite imagery by Maxar technologies, from Google Earth)

and Associates, 2020) and processed using the plug-in Griddle (Itasca 2021b) in order to create a volumetric mesh that could be imported directly into 3DEC.

The orientation of the discontinuities representing the release surfaces of the rockslides in the 3DEC model were obtained directly from the post-failure point cloud, by measuring the dip and dip direction of the rear and lateral release surfaces and defining the origin of the planes based on their true location within the slope. The orientation of the basal release surface, which is not visible in the field and the SfM model, was inferred through the combined interpretation of structural mapping procedure and kinematic analysis results, to identify the set(s) that most likely may have formed it. Multiple geological structures could have acted as basal surfaces, and two scenarios were therefore created to separately investigate the contributions of the identified structures in the failure. The code and model geometry used for this simulation will be made available on the institutional repository of the University of Bologna.

Results

Lineament mapping analysis

In total, 978 lineaments were derived from the manual mapping in ArcGIS and their bearing data imported in Dips to be plotted in a rosette diagram. Two major lineament trends were identified, striking 030°−040° and 140°, referred to as L1 and L2, respectively, in good agreement with lateral and rear release surfaces (Fig. 6). A third, E-W trending lineament orientation, referred to as L3, with an approximate 100° strike, was less frequently observed. These measured lineament orientations align closely with the main regional tectonic structures and physiographic features, particularly the Owl Creek Fault and the Joffre Creek (which form the Joffre Lakes west of the peak). Since the area investigated in this study is located within the hanging wall of the Owl Creek Fault, it is likely that the structures are associated with such structural alignment and that resulted from tectonic stresses due to bending, folding, and shearing that occurred during the displacement along the fault ramp. Other physiographic features of the investigated area, such as the Cayoosh Creek and Twin One Creek valleys, which strike in a 030° direction, may be controlled by geological structures related to tear faulting in the hanging wall (Fig. 6).

Discontinuity data and kinematic analysis

Using the high-resolution, helicopter-based SfM model, we mapped 472 discontinuities, 92 with a persistence greater than 50 m (1st order discontinuities) and 380 with a persistence less than 50 m (2nd order discontinuities). Discontinuities were grouped in seven discontinuity sets (D1-D7). Table 2 summarizes the average orientation of each set derived from the slope-scale and the window-scale

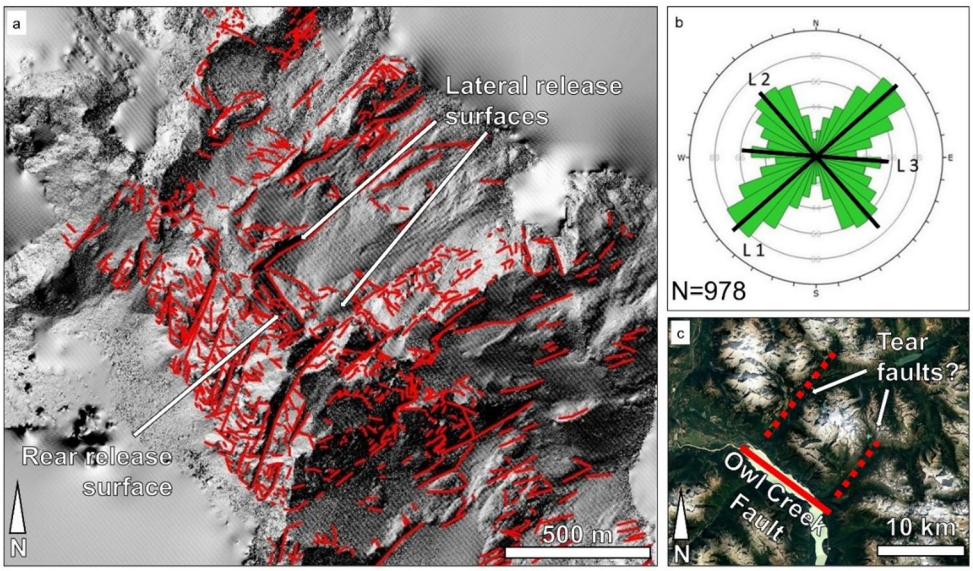


Fig. 6 Summary of the lineament analysis conducted using the post-failure model. (**a**) Map of the lineaments digitized across the investigated area. (**b**) Rosette plot showing the trend of the mapped lineaments. Each bar is 10° wide, and each circle represents 22 lineaments. Note the agreement between the lateral and rear release surfaces shown in a) with L1 and L2, respectively. (**c**) Interpretation of the correlation between lineament set L2 and two potential tear faults perpendicular to the Owl Creek Fault, which control the orientation of the Lillooet Lake (2020 satellite photograph by Maxar technologies, from Google Earth)

Table 2 Summary of the average orientation of the discontinuity sets mapped in the post-failure 3D model, expressed in dip direction (DD) and dip (D) 1 st order discontinuities are derived from slope-scale mapping, whereas 2nd order discontinuities are derived from window-scale mapping

SET ID	1 st order discontinuities (trace length > 50 m) DD/D	2nd order discontinuities (trace length < 50 m) DD/D
D1	115°/83°	129°/77°
D2	263°/35°	253°/48°
D3		225°/89°
D4	184°/42°	174°/57°
D5	071°/38°	-
D6	002°/17°	036°/37°
D7	113°/48°	103°/40°

discontinuity mapping. In general, good agreement is observed between the orientation of 1 st and 2nd order discontinuity sets. However, discontinuity set D3 was not recognized in the slope scale analysis, whereas discontinuity set D5 was not identified in the window scale analysis.

The mapped discontinuity sets can be correlated with the release surfaces of the Joffre Peak landslide events. In particular, the lateral release surface, characterized by an orientation of 135°/75°, can be ascribed to set D1, which has been observed at both window and slope scales (Fig. 7). Conversely, the rear release surface, characterized by an orientation of 50°/71°, correlates with 2nd order discontinuity set D3. However, no similarly oriented features were observed among 1 st order discontinuities. It is worth noting that the rear release surface is characterized by a distinct stepped morphology, which may have resulted from a progressive coalescence of multiple 2nd order, D3 discontinuities. As stated previously, compared to the rear and the lateral release surfaces, the identification of the structures controlling the orientation of the basal release surface is particularly challenging, due to the presence of landslide debris cover (Fig. 2). Based on the assumption that the slope of the debris deposit covering the basal surface is controlled by the underlying geological structure, the surface deposit orientation was measured and an average value of 036°/30° was also recorded (Fig. 8), similar to discontinuity set D6 (2nd order).

In order to identify the discontinuity sets that may have contributed to the development of the basal surface, a detailed kinematic analyis has been performed, which also considered the variation in slope orientation that occurred after the detachment of the first landslide on May 13th, 2019 (Fig. 9). For the kinematic analysis of the first landslide (i.e., failure of the landslide Block 1), performed in Dips, a slope dip direction of 45° and a dip angle of 80° (derived from the pre-landslide 3D terrain model) were assumed. An effective angle of friction of 10° was considered for all discontinuities, in order to indirectly consider the impact of the high porewater pressure that has been suggested to have been present prior to the failure (Friele et al. 2020). It is worth noting that traditional, stereonet-based kinematic analyses do not allow water pressure in discontinuities to be explicitly implemented, as water pressure produces a reduction in effective stresses, rather than friction angle. However, considering a reduced, effective friction angle in kinematic analyses can allow the impact of water pressure to be indirectly and conceptually considered by reducing the overall

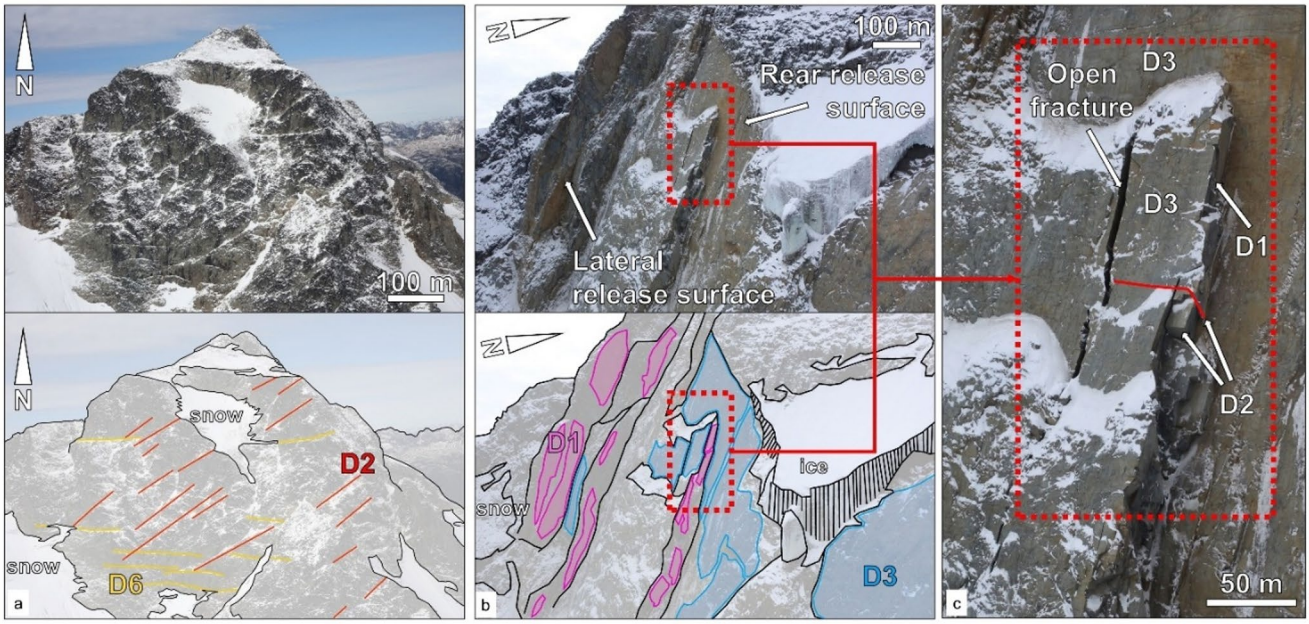


Fig. 7 Summary of the main discontinuity sets observed at the Joffre Peak. (**a**) Photograph and simplified structural interpretation of the southern slope of the Peak. Selected traces of discontinuity sets D2 and D6 (striking approximately perpendicularly to the slope) are shown. The area depicted in the photograph is about 400 m wide. (**b**) Photograph and simplified structural interpretation of the upper part of the landslide scar, showing the lateral and rear release surfaces of landslide Block 2 controlled by discontinuity sets D1 and D3, respectively. (**c**) potentially unstable columnar block on the back-scarp surface, approximately 50 m wide. The structures defining the blocks, including the potential base formed by D2, are shown. Note the width of the tensile crack that enlarges in the upper part, denoting a possible toppling displacement that resembles, albeit at a smaller scale, that of landslide Block 2

resistance to sliding along planar and wedge basal surfaces. Additionally, it allows the effects of different kinematic configurations to be more clearly highlighted. A lateral limit of 20° was set for planar sliding and direct toppling. Kinematic analyses show that planar sliding along discontinuity set D6 is kinematically feasible considering both 1 st order and 2nd order discontinuities (Fig. 9a). Sets D1 and, to a lesser extent, D4, D5, and D7 are all capable of acting as lateral boundaries of sliding blocks. Discontinuity set D6 can also potentially act as basal surface for block toppling failures, with friction mobilized along discontinuity sets D2 and D3 dipping into the slope (Fig. 9c). At this regard, a preliminary analysis performed using the Choquet and Tanon's nomograms, which uses the various dimensions of the block to evaluate its stability and kinematic failure mechanism (Choquet and Tanon 1985), provided a factor of safety (FS) close to 1 for a block 180 m high and 50 m wide with an assumed interslice friction angle of 20°. In terms of wedge sliding, various intersections were observed that can potentially form unstable wedges. In most cases, wedges result from the combination of discontinuity set D6 with D4, D2, D7, as well as discontinuity set D1. The latter set, however, in view of the high dip angle, acts more as lateral constraint for blocks sliding along D6, rather than a true basal surface. Additionally, the possibility of rotation of high angle wedges cannot be ruled out (Fig. 9e; Steffen O.K.H. 1978).

The change in slope kinematics that followed the first landslide event was investigated by performing a new kinematic analysis considering a new, post-failure slope surface orientation. Such post-failure slope surface was assigned a dip direction of 315° and a dip angle of 90°, which also represents the structural surface separating the two landslide blocks (Fig. 2). The graphical representation of such a complex slope orientation was achieved by merging the instability envelopes for the two slope face orientations (Fig. 9b, d, f). For the planar sliding case, in order to merge the instability envelopes, the lateral limit for the second event was extended in the southerly direction, in order to account for the enhanced kinematic freedom that existed between the north- and the east-facing parts of the slope between May 13th and May 16th. In other words, full kinematic freedom for planar sliding in directions between 315° (to the NW) and 45° (to the NE) was considered. Also in this case, a 10° effective friction angle was assumed for all discontinuities.

When considering the new slope orientation, an increased likelihood of wedge instability is noted, due to the potential block sliding along the intersections between D2 (which was observed at both the window and slope scale) and D6. The feasibility of wedge sliding along such intersection increased significantly after the first landslide, because the trend of the line of intersection changed from sub-parallel to the slope face before the first event to normal to the slope

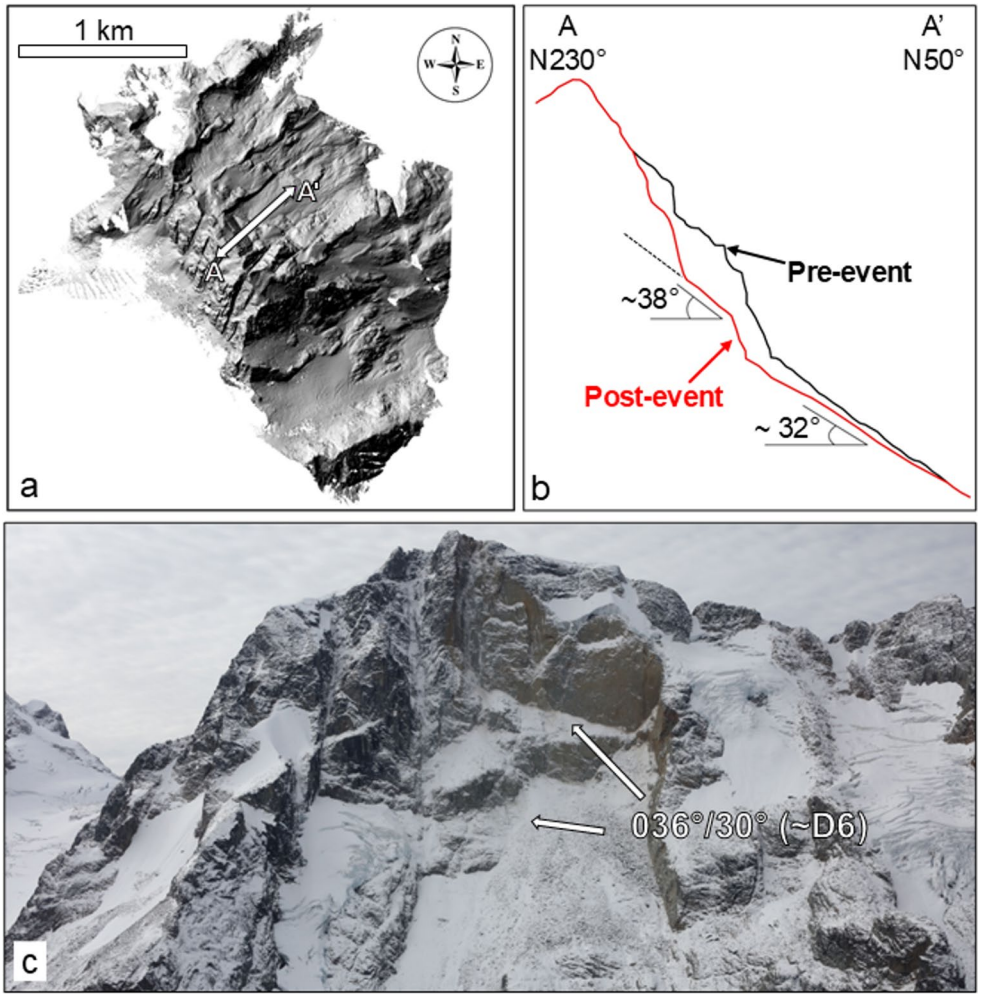


Fig. 8 Preliminary interpretation of the basal surface based on the slope of the debris cover. The orientation of the debris slope, in the hypothesis that it is controlled by the underlying structural surface, is similar to set D6. (**a**) the position of the cross section in (**b**) is shown using the post-failure hillshade raster as a basemap. **b**) cross section showing the change in morphology before and after the first event. (**c**) areas where the orientation of the debris slope were measured (assuming a correlation with an underlying structurally-controlled basal surface. The measured orientation is similar to D6 (cfr. Table 2)

face after the first event. The residual, potentially unstable columnar block visible along the present-day sub-vertical release surface (Fig. 7c), may represent a small-scale example of the failure mechanism that characterized the second landslide event. The base of this 50 m tall and 20 m wide columnar block is formed by a persistent D2 discontinuity. Such a significant change in kinematic freedom, compared to other wedge intersections, suggests that it may have controlled the stability of the second block more effectively than any other intersection, particularly after the detachment of the first landslide. Therefore, it was decided to further investigate this feature using numerical modelling.

3D numerical modeling

The objective of 3D numerical modelling was to investigate the role of kinematics and discontinuity intersections on the stability and evolution of the Joffre Peak slope. Additionally, in view of the structurally controlled nature of the landslides, and the limited impact of rock mass yielding and internal deformation on the initial detachment of the landslide blocks, a rigid-block approach was considered fit for purpose.

Kinematic analyses evidenced that the first landslide likely failed through a planar sliding mechanism. The displacement of the landslide Block 2 may also have occurred through a planar sliding mechanism; however, its delayed detachment may indicate differences in the characteristics of its basal surface, which can be ascribed to (A) local changes in the continuity or persistence of the basal surface (i.e., increased roughness or rock bridge percentage) of the landslide Block 2, or (B) to a change in failure mechanism, following the increased kinematic feasibility of wedge instability after the detachment of the landslide Block 1. These two possible scenarios (A and B) were investigated using numerical modelling. In scenario A, the two landslide blocks displace along the same basal surface, constituted by a D6 discontinuity. In scenario B, the landslide Block 2 fails through a wedge sliding mechanism, displacing along the line of intersection between discontinuity sets D6 and D2, which are assumed to form the basal surface of landslide Block 2 (Fig. 10b). It is worth noting that, when a basal

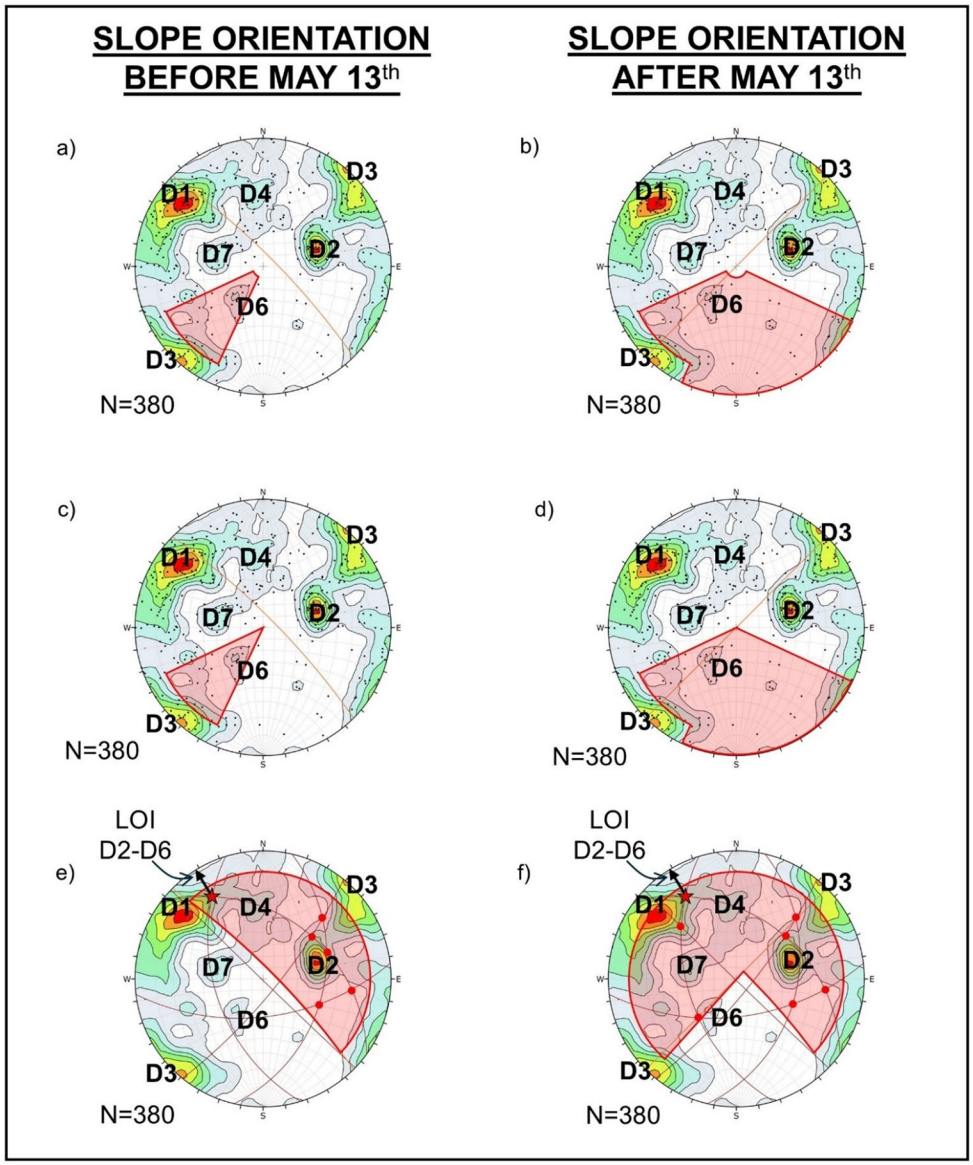


Fig. 9 Stereonets illustrating the Joffre Peak slope kinematic analysis before and after the failure of landslide Block 1. For the analysis in the post May 13th configuration, the instability envelopes of both slope orientations have been merged. For clarity, only poles to 2nd order discontinuities have been included. **a**, **b**) Planar sliding analysis. In **b**), the lateral limit on the southern side was extended to account for the kinematic freedom provided by the east-facing part of the slope. **c**, **d**) Block toppling analysis. **e**, **f**) Wedge sliding analysis. The red star represents the intersection between D2 and D6 that was considered for subsequent numerical modelling. Note the transition of the line of intersection (LOI) from a sub-parallel orientation (prior to the first landslide) to a normal orientation to the slope face (after the first landslide)

surface with the same properties and geometry is considered for both landslide blocks, a multi-stage failure cannot be simulated, therefore, such a scenario is not presented in this study.

Additionally, the analyses were performed assuming dry conditions, due to the lack of groundwater data, and no water pressure was explicitly considered. This approach was considered appropriate, as the main objective of this study was to investigate the role of slope kinematics, rather than the environmental controls (e.g., permafrost degradation and subsequent increase of pore water pressure, ice-jacking and water pressure build-up in fractures, e.g., Brideau et al. 2005; Haeberli et al. 1997).

Based on the results of the kinematic analysis and the mapping of the post-failure SfM model, the bounding discontinuities of the landslide blocks were explicitly implemented in the 3DEC geometry. Specifically, the high persistence discontinuities that acted as backscarp (050°/71°), lateral release surfaces (135°/75°), basal surface (036°/30°), which can be ascribed to sets D3, D1, and D6, respectively, were considered. In scenario B, a D2 discontinuity was also included with an orientation of 270°/40°. In both scenarios, the model is ultimately constituted by two blocks ("Block 1" and "Block 2"), which represent the volumes failed during the two landslide events (Fig. 10a).

Both scenarios were initially simulated in 3DEC with joint stiffness parameters, friction angle and cohesion, only applied to the detachment surfaces, to recreate the distribution of initial pre-failure stresses and elastic deformations along the discontinuities. The detachment of landslide Block 1 was then simulated by assigning a Mohr-Coulomb constitutive model (i.e., elastic-perfectly plastic behavior)

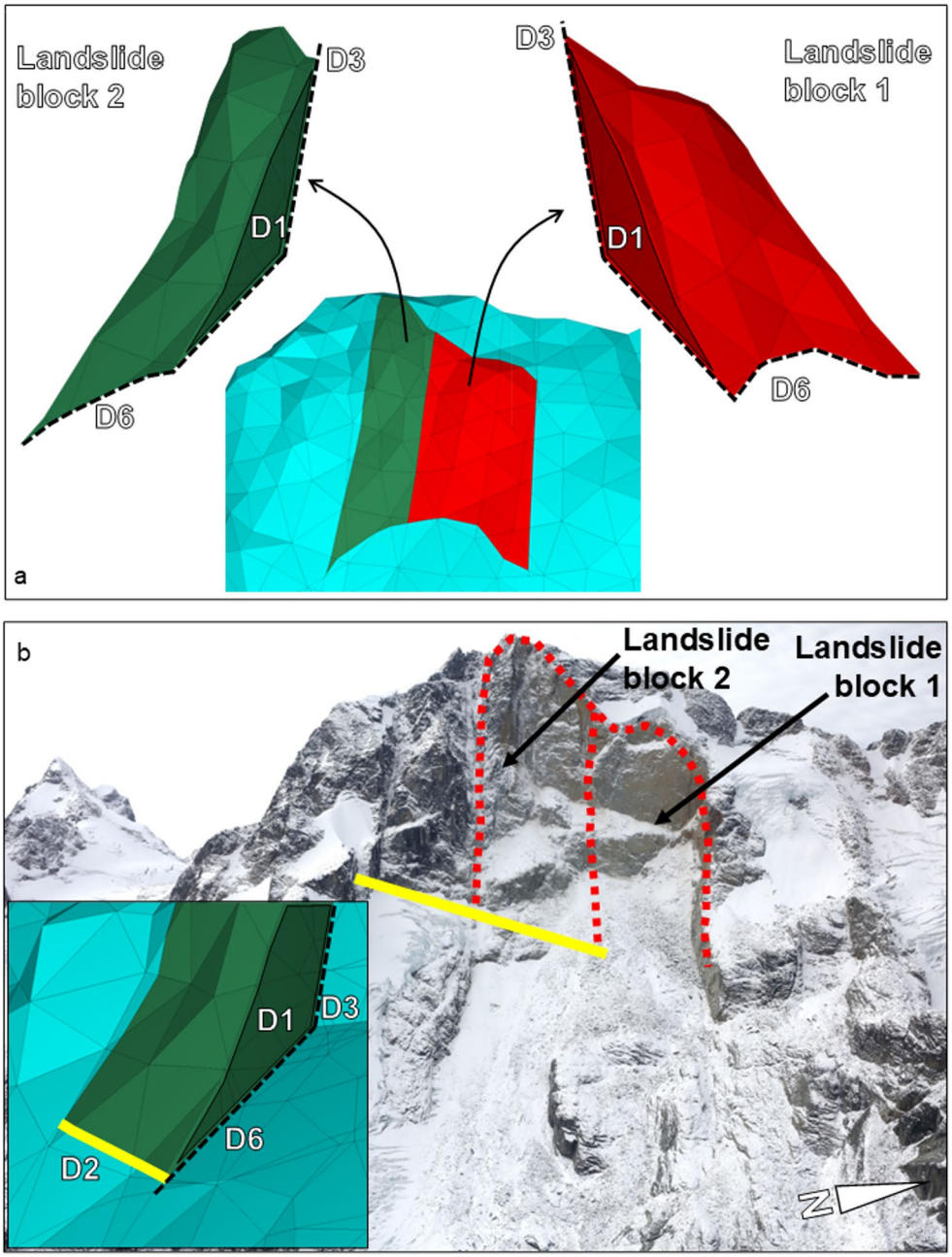


Fig. 10 Overview of the numerical model geometry. (**a**) Block diagram of the model in 3DEC. The two landslide events are labelled as "landslide Block 1" and "landslide Block 2". (**b**) Detail of the basal surface of landslide Block 2 in scenario B. Note the intersection between D2 and D6 inducing the development of a wedge sliding mechanism. In scenario A, D2 is not implemented, and both landslide blocks are assumed to slide along D6

to the discontinuities and progressively decreasing the friction angle. As the landslide blocks were assumed to be rigid and non-deformable, only the density value was assigned to the rock mass. Table 3 summarizes the input parameters assigned to the material and the discontinuity surfaces.

Scenario A

In this scenario, the delay after which the second landslide occurs is assumed to be due to a higher amount of rock bridges that require fracturing in order to allow displacement. The higher amount of rock bridges (or a locally higher surface roughness) along the basal surface of landslide Block 2 is implicitly accounted for by assigning a higher value of cohesion to the surface, which was then progressively reduced from 10 MPa to 0 MPa (simulating fracture propagation and coalescence; Table 3) until unstable conditions were achieved. This approach, initially introduced by Terzaghi (1962) and Jennings (1970), is often used in practice to simulate the presence of non-persistent discontinuity surfaces in numerical simulations (e.g., Kemeny 2005; Stead and Eberhardt 2013; Bonilla-Sierra et al. 2015; Delonca et al. 2020; Sampaleanu 2017). The other

Table 3 Summary of the material properties assigned to rock mass and discontinuities for the investigated scenarios. In both scenarios, friction angle is progressively reduced in stage 1 until block 1 becomes unstable. In scenario B, cohesion is progressively reduced until block 2 becomes unstable. See text for details

Model feature	Property	Stage 1	Stage 2
Rock mass (undeformable)	Density	2600 kg/m^3	2600 kg/m^3
Discontinuities (Mohr-Coulomb constitutive model)	Friction angle	25° (progressively decreased to 12° until failure of block 1)	12° (11° for D2)
	Cohesion (base of Block 1)	0 MPa	- (landslide Block 1 removed)
	Cohesion (Base of Block 2)	10 MPa	10 MPa (reduced until failure of landslide Block 2)
	Joint normal stiffness	100 MPa/m	100 MPa/m
	Joint shear stiffness	10 MPa/m	10 MPa/m

discontinuities, including the basal surface of landslide Block 1, were assumed to be cohesionless.

The analysis was performed by progressively decreasing the friction angle from 25° to 10°. The failure of landslide Block 1 was simulated for a friction angle of 12° (Fig. 11). Due to the higher cohesion, landslide Block 2 appears to be stable. Only after the detachment and removal of the first landslide (i.e., landslide Block 1) after a displacement of about 19 m, the failure of landslide Block 2 could be replicated in the model, after progressively reducing the cohesion. Failure is simulated as a planar sliding with a limited component of backward tilting, in view of the higher simulated displacement magnitude in the lower part of the block.

Scenario B

In scenario B, the geometry of the basal surface of landslide Block 2 was modified, by including the additional D2 discontinuity surface (270°/40°), resulting in an increased feasibility of a wedge sliding failure for the second landslide (Fig. 10b). During the simulation, the friction angle of the basal surface was again progressively decreased from 25° to 10°. Similar to scenario A, the failure of the landslide Block 1 occurred for a value of friction angle of 12° (Fig. 11).

After a displacement of about 11 m, landslide Block 1 was considered to have failed and was removed from the model. Then, cohesion along the basal surface of landslide Block 2 was progressively reduced. As cohesion was set to 0 MPa, landslide Block 2 began displacing into the empty space left by landslide Block 1 (Fig. 11). The simulated movement predominantly occurs as a wedge sliding along D2 and D6 intersection, with a relatively larger displacement becoming apparent in the lower portion of Block 2, suggesting also in this scenario a backward rotational component that remains, however, of secondary importance.

Discussion

The analysis of the collected data shows that the rock mass forming the Joffre Peak is characterized by several discontinuity sets that are distinguished by a high variability in orientation. The agreement between the major lineament trends and the 1 st and 2nd order discontinuity sets demonstrates a strong control of geological structures at various scales on the geomorphological setting of the area, including the orientation of ridges, gullies, and creeks. At the slope scale, the lateral and rear kinematic release surfaces for both landslide blocks were provided by the discontinuity sets D1 and D3, respectively. Discontinuity set D3 was more frequently observed at the window-scale (i.e., 2nd order discontinuities), than at the slope-scale (i.e., 1 st order discontinuities). In particular, relatively shorter trace lengths were observed within mapping window 1, located on the rear slope of Joffre Peak. Here, a markedly stepped morphology, caused by the progressive detachment of smaller blocks over time, enhances the visibility of persistent D1 discontinuities in contrast to a more limited apparent persistence of set D3. The higher trace length and persistence of D1, compared to D3, could also be related to the different tectonic processes and related stresses by whom they were respectively generated. In this perspective, the agreement between the orientation of set D1, the lineament trend L1, and the structurally controlled physiographic lineaments (i.e., Joffre Creek and Twin One Creek) suggests that all these features are linked to tectonic faulting.

Despite the good visibility of the lateral release surface, and the presence of a photographic record showing the conditions of the slope prior to and after the events, as well as after the first landslide event, the kinematic interpretation of the slope instability and its evolution remains challenging, largely because of the debris deposit that covers the basal surface preventing direct observation and orientation measurement. An “indirect investigative approach” was needed

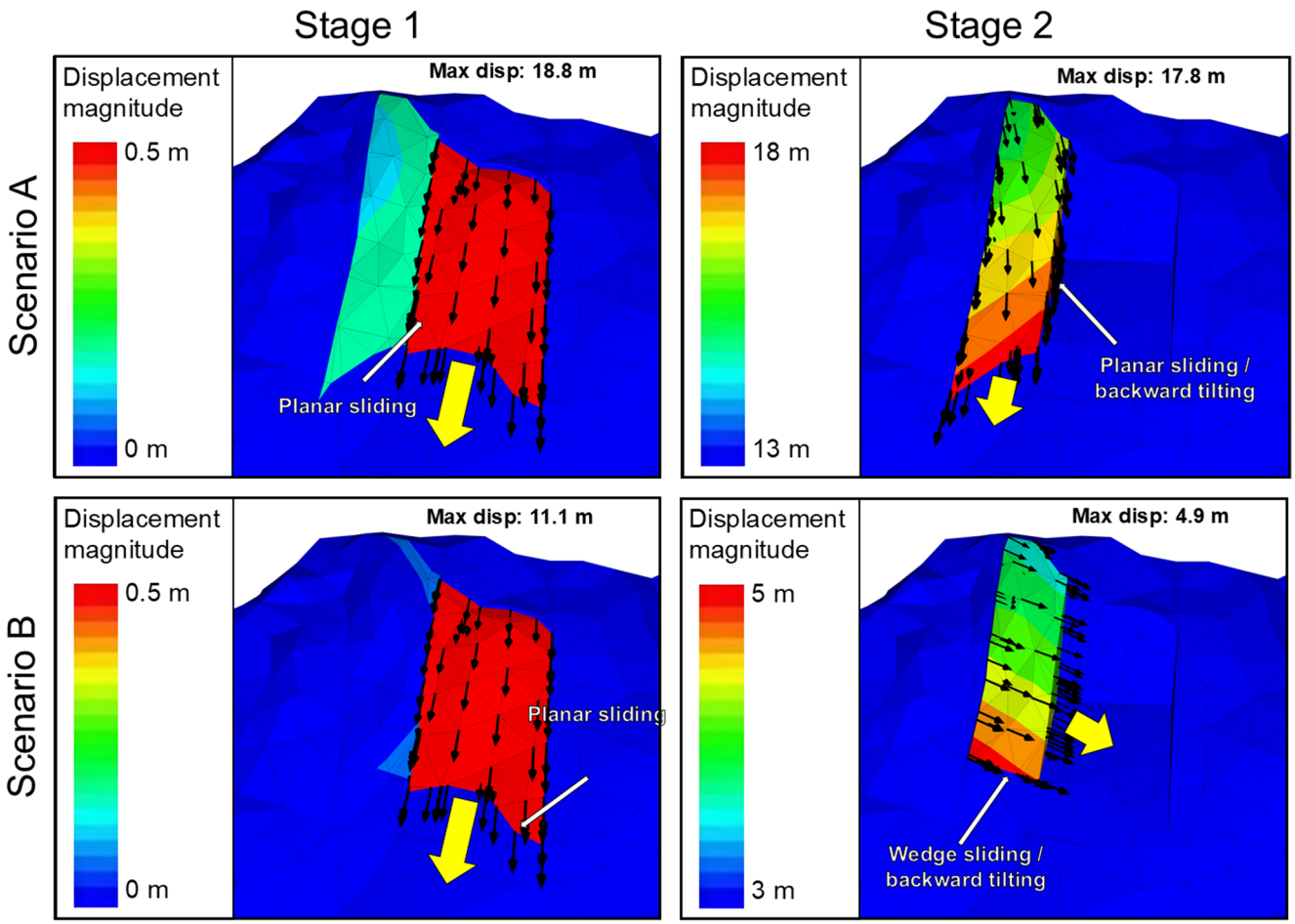


Fig. 11 Summary of the results of 3DEC numerical simulation, with reference to displacement magnitude. Yellow arrows show the principal direction of displacement of the unstable blocks. In stage 1 landslide Block 1 fails, in both scenario A and scenario B, through a planar sliding mechanism. In stage 2, after the removal of landslide Block 1, landslide Block 2 in scenario A fails through a mixed planar sliding mechanism with a backward tilting component, whereas in scenario B a wedge sliding is simulated. In both scenarios, landslide Block 2 shows a component of displacement towards the void left by the detachment of landslide Block 1. Moreover, in view of the slenderness of the block, an evolution towards a toppling cannot be excluded

to infer which discontinuity set may have controlled the basal surface.

Kinematic analysis considering the original slope surface showed that the failure of the landslide Block 1 was likely due to a planar sliding along discontinuity set D6. This interpretation is also supported by the similarity between the average orientation of discontinuity set D6 (Fig. 9) and the slope of the debris deposit covering the basal surface, which is arguably controlled by the orientation of the underlying structural discontinuity The orientation of other discontinuity sets identified in the course of the geomechanical mapping is not capable of providing adequate kinematic freedom for the failure through planar sliding of landslide Block 1. The kinematic analysis for wedge sliding also showed some potentially unstable intersections. However, the majority of them entail a sliding component occurring mostly along D6 discontinuities with other discontinuity sets acting as lateral boundaries (e.g., D1, D4, D7). Only the wedge intersection between D2 – D4 falls within the toppling envelope implying a possibility of rotation of high angle wedges.

The failure mechanism of landslide Block 2 is more complex. Its failure occurred with a 4-day delay from the failure of landslide Block 1, which left the slope close to a limit equilibrium condition. Two scenarios were hypothesized to explain such behavior. In one case (scenario A), the delay represented the time required for rock bridge or asperity shearing along the basal surface, which is shared with landslide Block 1. The mechanical process controlling this progressive failure behavior can be ascribed to a sub-critical crack growth, which can result in the brittle fracturing of intact rock along the incipient rupture surface. This process has been described numerically by Kemeny (2005), among others, and entails the propagation of pre-existing fractures within intact rock for stress magnitudes lower than the strength of the intact material. The second scenario involves sliding (later combined to a lesser extent with backward

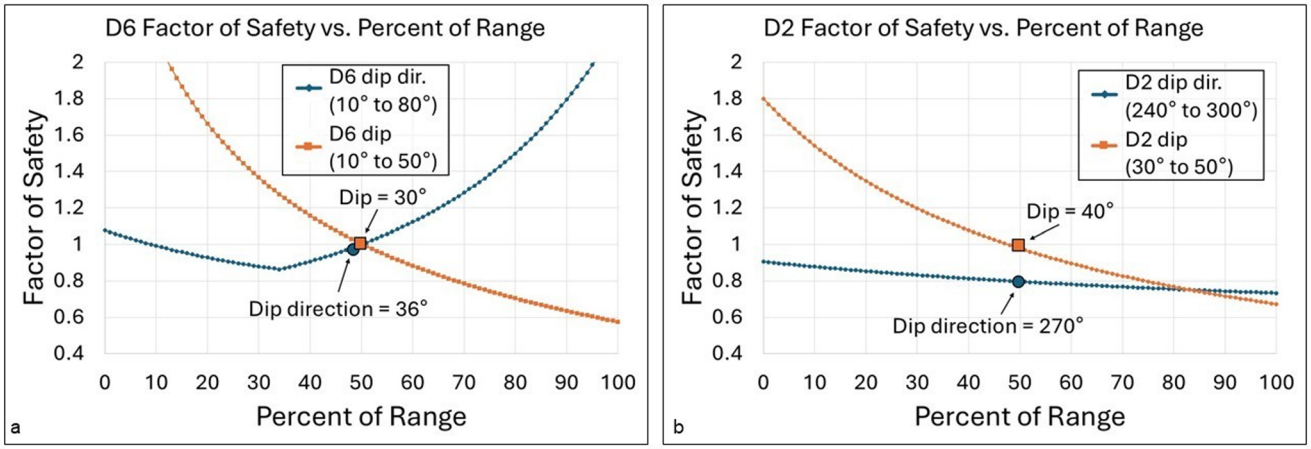


Fig. 12 Overview of the preliminary sensitivity analysis conducted in SWedge. a) effects of change in orientation of D6 (which acts as basal surface for landslide Blocks 1 and 2 in scenario A, and for landslide Block 1 in scenario B. b) effects of changes in orientation for D2 discontinuity at the base of landslide Block 2 in scenario B. The larger markers indicate the values of dip and dip direction used in the 3DEC models

tilting due to the slenderness of landslide Block 2) along the intersection between discontinuity sets D6 and D2.

In both scenarios, in view of the low steepness of the basal discontinuity, a relatively low angle of friction (12° for the basal sliding surface of landslide Block 1) had to be assigned to simulate failure. It should be noted that the presence of a steeper basal surface for both landslide blocks cannot be presently ruled out, since the surface is not presently visible. However, neither the geomechanical data derived from the multi-scale slope characterization nor the profile traced through the landslide area show evidence of any single geological structure or discontinuity sets that could form a steeper basal surface.

From a kinematic perspective, landslide Block 1 represented a key-block within the rock slope, as the displacement of landslide Block 2 shows a component of displacement towards the void left by the first event in both the investigated scenarios (Fig. 11). Based on this observation, it is evident that, after the detachment of landslide Block 1, a certain degree of stress concentration must have occurred along the base of landslide Block 2, which in turn could have promoted shearing of asperities and/or rock bridges. This, however, does not necessarily imply any spatial variation in roughness of rock bridge intensity between the basal surfaces of the two landslide blocks, at least in their initial conditions. In fact, a greater concentration of shear stresses likely affected the basal surface of landslide Block 1, due to its greater kinematic freedom compared to landslide Block 2, which was at least in a partly tapered condition before the occurrence of the first event. Even considering a similar roughness or rock bridge content along the base of landslide Block 1 (and therefore a similar initial strength), the increased stress concentration, maintained over the long term, may have likely caused a faster strength decrease ultimately leading to the failure of the block. After the detachment of landslide Block 1, a limited kinematic constraint existed for landslide Block 2, causing shear concentration along its basal surface to increase. Ultimately, such a change in stress concentration led to the detachment of landslide Block 2 after achieving a condition of kinematic freedom, following rock bridge and asperity shearing, possibly through sub-critical crack growth.

It is clear that scenario A implies the development of a damage-controlled progressive failure. Such a process, however, cannot be ruled out for the wedge sliding failure mechanism depicted in scenario B. In fact, currently available data and information do not allow either scenario to be considered as the more realistic one. A combination of the two cases (i.e., a partial tapering of landslide Block 2 controlled by non-persistent D2 discontinuities dipping into the slope, along the basal surface) can also represent a realistic solution.

Preliminary sensitivity analyses were conducted on a simplified geometry, using a Limit Equilibrium (LE) method in SWedge (RocScience, 2023) aimed at investigating how variations in the orientation of discontinuities forming the basal surfaces of landslide Blocks 1 and 2 can impact overall stability and behavior of the slope. With regard to stage 1 of both scenarios, we observe that Factor of Safety (FS) tends to decrease as the dip direction of D6, reaching its minimum for a dip direction of 54° (Fig. 12). This observation is also valid for stage 2 in scenario A, as the orientation of the basal surface is the same for both landslide Blocks 1 and 2. Conversely, when considering stage 2 for scenario B, the introduction of a discontinuity D2 forming the basal surface increases the complexity of the analysis. This simplified analysis showed that the FS is marginally impacted by the dip angle of D2, which remains largely unchanged

within a range of values between 30° and 50°. Conversely, the FS rapidly decreases as the dip direction of D2 varies from 240° to 300°. Note that in the model the orientation of the controlling discontinuities was chosen based on the results from the kinematic analysis (i.e., using orientation data of mapped discontinuity sets), in order to maintain consistency between field data and model geometry.

Further insight could be provided by more advanced numerical analyses, capable of simulating progressive damage accumulation and its effect on block displacement (e.g., FDEM). However, this additional analysis is beyond the scope of this study. Nonetheless, it is possible to speculate as to which are the processes that controlled damage development along the basal surfaces of both landslide blocks, which ultimately played an important role in defining the evolution of instability of the rock slope. The 2019 Joffre Peak landslides affected a high angle, sub-vertical rock slope, which likely resulted from a combination of glacier erosion and oversteepening, and the subsequent instability due to decreased lateral support following deglaciation (e.g., Clague and Evans 1994). Geomorphic setting represents the first important predisposing factor on the 2019 multi-stage event, as it can potentially promote stress concentration and progressive damage accumulation at the base of high rock slopes, even when made of high-quality rock mass (e.g., Barton and Shen 2018; Fan et al. 2019). Ongoing climate change and the subsequent widespread permafrost degradation phenomena have also been often linked to similar large slope failures occurring at high altitudes in Canada (Geertsema et al. 2006; Roberti et al. 2018), Western China (Fan et al. 2019), in the Swiss Alps (Gschwind et al. 2019), and Chilean Andes (Sepulveda et al. 2023). In fact, Friele et al. (2020) suggested a potential contribution of ongoing climate change and permafrost degradation on the occurrence of the Joffre Peak landslides. In their work, however, they observe that permafrost degradation cannot be undoubtedly linked to the failure, based on the limited available data on its distribution across the region. Nonetheless, based on data collected at weather station in the vicinity of the site, they observed that temperature, following an extended below-freezing period, remained constantly above 0° for the week prior to the failure, leading to a significant snow-melt between May 7th and May 14th. The results of our analysis are seemingly in agreement with their observations. The low value of friction angle (12°) assigned to the basal surface of landslide Block 1 in 3DEC can be justified by the presence of a relatively high water pressure at the time of the failure (which was not explicitly considered in the model), regardless of its origin. It is clear that slope kinematics, which is commonly linked to structural geology, and, to an extent, long-term geomorphic slope evolution, can also be indirectly controlled by short-term environmental and climatic processes that can cause an increase in damage accumulation rates or temporary increases in water pressure within rock slopes. Damage accumulation processes, in turn, can locally enhance kinematic freedom (e.g., Donati et al. 2023), ultimately resulting in the development of major slope instabilities.

Conclusions

In this work, a combined remote sensing-numerical modeling approach is employed to investigate the failure of a multi-stage rock slope failure and the role that geological structures and changes in slope kinematics played in its evolution. The collection and processing of geological and structural data posed significant challenges, in view of the complex geomorphic and structural configuration of the slope, its inaccessibility, and the limited visibility of the basal release surface due to landslide debris and snow cover. The use of remote sensing techniques, namely helicopter-based SfM, allowed collection of structural and geomechanical data. Our analysis highlighted the role that the different discontinuity sets in controlling the instability of the Joffre Peak slope. A multi-temporal kinematic analysis approach was applied, in which the slope surface orientation is varied so as to replicate the progressive geomorphic evolution of the slope. It is noted that:

- landslide Block 1 failed as a planar sliding and was laterally constrained by sub-vertical highly persistent discontinuities;
- the mechanism through which the detachment of landslide Block 2 occurred cannot be definitively identified. Landslide Block 2 may have failed either as a translational planar slide (similar to the first event), or through a mixed wedge sliding - backward tilting mechanism, with a displacement direction towards the void space left by the removal of landslide Block 1.

3D discontinuum modelling was used to back-analyze the failure; the results indicated that landslide Block 1 represented a key-block for the slope. Regardless of the failure mechanism, simulations showed that the displacement of landslide Block 2 occurred towards an empty void resulting from the removal of landslide Block 1.

The analysis of the Joffre Peak landslides also suggests that the combined effect of variations in environmental or climatic conditions and the geomorphic evolution and steepening of local topography can play a role in controlling not only the stability of rock slopes, but also their kinematics, by promoting damage accumulation and progressively

reducing the strength of rupture surfaces and thereby the kinematic constraint of incipient landslides.

Ultimately, our research shows that not only is kinematic analysis useful as a method to preliminarily assess rock slope stability but also represents an important tool in the investigation of multi-stage landslides, particularly those controlled by geological structures at various scales. However, the interpretation of the results should not merely take into consideration the orientation of the discontinuities bounding the investigated blocks. The shape of the block, its slenderness, and the occurrence of complex intersections should be taken into account, when possible, to effectively evaluate the changes in mechanism and displacement over the course of the slope deformation and failure.

Acknowledgements The authors gratefully acknowledge Emre Önsel and Omar Chang for the technical discussions in SFU lab and Gioachino Roberti for assistance during the helicopter survey.

Funding Open access funding provided by Alma Mater Studiorum - Università di Bologna within the CRUI-CARE Agreement. This work was supported by a scholarship provided by University of Ferrara to the first author by the Atlante program funds 2019. The authors would also like to acknowledge financial support provided through an NSERC Discovery Grant (ID: RGPIN 05817) and FRBC Endowment funds provided to Doug Stead.

Declarations

Competing interests The authors declare that they have no conflict of interest.

Open Access This article is licensed under a Creative Commons Attribution 4.0 International License, which permits use, sharing, adaptation, distribution and reproduction in any medium or format, as long as you give appropriate credit to the original author(s) and the source, provide a link to the Creative Commons licence, and indicate if changes were made. The images or other third party material in this article are included in the article's Creative Commons licence, unless indicated otherwise in a credit line to the material. If material is not included in the article's Creative Commons licence and your intended use is not permitted by statutory regulation or exceeds the permitted use, you will need to obtain permission directly from the copyright holder. To view a copy of this licence, visit http://creativecommons.org/licenses/by/4.0/.

References

Agisoft LLC (2022) Metashape Professional (Version 2.0). Available online: http://www.agisoft.com/ (accessed on 15 January 2024)

Bar N, Borgatti L, Donati D, Francioni M, Salvini R, Ghirotti M (2021) Classification of natural and engineered rock slopes using UAV photogrammetry for assessing stability. IOP Conf Ser Earth Environ Sci 833:1–7. https://doi.org/10.1088/1755-1315/833/1/012046

Barton N, Shen B (2018) Extension strain and rock strength limits for deep tunnels, cliffs, mountain walls and the highest mountains. Rock Mech Rock Eng 51:3945–3962. https://doi.org/10.1007/s00603-018-1558-2

Bonilla-Sierra V, Scholtès L, Donzé FV, Elmouttie M (2015) DEM analysis of rock bridges and the contribution to rock slope stability in the case of translational sliding failures. Int J Rock Mech Min Sci 80:67–78. https://doi.org/10.1016/j.ijrmms.2015.09.008

Bozzano F, Lenti L, Martino S, Montagna A, Paciello A (2011) Earthquake triggering of landslides in highly jointed rock masses: reconstruction of the 1783 Scilla rock avalanche (Italy). Geomorphology 129:294–308

Brideau MA, Stead D, Kinakin D, Fecova K (2005) Influence of tectonic structures on the Hope Slide. Br Columbia Can Eng Geol 80(3–4):242–259. https://doi.org/10.1016/j.enggeo.2005.05.004

Brideau MA, Yan M, Stead D (2009) The role of tectonic damage and brittle rock fracture in the development of large rock slope failures. Geomorphology. https://doi.org/10.1016/j.geomorph.2008.04.010

Brideau M-A, Pedrazzini A, Stead D, Froese C, Jaboyedoff M, van Zeyl D (2011) Three-dimensional slope stability analysis of south peak, Crowsnest pass. Alta Can Landslides 8:139–158. https://doi.org/10.1007/s10346-010-0242-8

Bromhead EN, Coppola L, Rendell HM (1996) Valley blocking landslide dams in the eastern Italian Alps. Proceedings of the 7th International Symposium on Landslides, Trondheim, Norway 17–21 June. Balkema, Rotterdam. pp 655–660

Bustin AMM, Clowes RM, Monger JWH, Murray Journeay J (2013) The southern Coast Mountains, British Columbia: new interpretations from geological, seismic reflection, and gravity data. Can J Earth Sci 50:1033–1050. https://doi.org/10.1139/cjes-2012-0122

Carlà T, Intrieri E, Di Traglia F, Nolesini T, Gigli G, Casagli N (2017) Guidelines on the use of inverse velocity method as a tool for setting alarm thresholds and forecasting landslides and structure collapses. Landslides 14:517–534. https://doi.org/10.1007/s10346-016-0731-5

Carlà T, Intrieri E, Raspini F, Bardi F, Farina P, Ferretti A, Colombo D, Novali F, Casagli N (2019) Perspectives on the prediction of catastrophic slope failures from satellite InSAR. Sci Rep 9:14137. https://doi.org/10.1038/s41598-019-50792-y

Carlà T, Gigli G, Lombardi L, Nocentini M, Gracchi T, Rossi G, Stefanelli TC, Raspini F, Fubelli G, Casagli N et al (2024) Mechanisms of Block Instability at the Toe of a Slowly Deforming Rock Slope. Rock Mech Rock Eng 57:1543–1563. https://doi.org/10.1007/s00603-023-03674-9

Casagli N, Frodella W, Morelli S, Tofani V, Ciampalini A, Intrieri E, Raspini F, Rossi G, Tanteri L, Lu P (2017) Spaceborne, UAV and ground-based remote sensing techniques for landslide mapping, monitoring and early warning. Geoenviron Disasters 4:1–23. https://doi.org/10.1186/s40677-017-0073-1

Cascini L, Cuomo S, Guida D (2008) Typical source areas of May 1998 flow-like mass movements in the Campania region, Southern Italy. Eng Geol 96:107–125

Choquet P, Tanon DDB (1985) Nomograms for the assessment of toppling failure in rock slopes. Proceedings of the 6th U.S. Symposium on Rock Mechanics (USRMS), 26–28 June, Rapid City, South Dakota

Cignoni P, Callieri M, Corsini M, Dellepiane M, Ganovelli F, Ranzuglia G (2008) others, Meshlab: an open-source mesh processing tool, Proceedings of the Sixth Eurographics Italian Chapter Conference. pp. 129–136

Clague JJ, Evans S (1994) Recent climatic change and catastrophic geomorphic processes in mountain environments. Geomorphology 10(1–4):107–128. https://doi.org/10.1016/0169-555X(94)90011-6

CloudCompare (2022) CloudCompare 2.12 [GPL Software]. Available online: https://www.cloudcompare.org/ (accessed on 15 January 2024)

Corkum AG, Martin CD (2004) Analysis of a rock slide stabilized with a toe-berm: a case study in British Columbia. Can Int J Rock

Mech Min Sci 41:1109–1121. https://doi.org/10.1016/j.ijrmms.2004.04.008

Crosta GB, Frattini P (2003) Distributed modelling of shallow landslides triggered by intense rainfall. Nat Hazards Earth Syst Sci 3:81–93

Cui Y, Miller D, Schiarizza P, Diakow LJ (2017) British Columbia digital geology. British Columbia Ministry of Energy, Mines and Petroleum Resources, British Columbia Geological Survey Open File 2017-8, 9p. Data version 2019-12-19. Retrieved from: https://www2.gov.bc.ca/gov/content/industry/mineral-exploration-mining/british-columbia-geological-survey/geology/bcdigitalgeology (accessed on April 24th, 2024)

Cundall PA (1988) Formulation of a three-dimensional distinct element model—Part I. A scheme to detect and represent contacts in a system composed of many polyhedral blocks. Int J Rock Mech Min Sci Geomech Abstr. https://doi.org/10.1016/0148-9062(88)92293-0

Delonca A, Gunzburger Y, Verdel T (2020) Cascade effect of rock bridge failure in planar rock slides: explicit numerical modelling with a distinct element code. Nat Hazards Earth Syst Sci Discuss 21(4):1–22. https://doi.org/10.5194/nhess-21-1263-2021

Donati D, Stead D, Brideau MA, Ghirotti M (2021) Using pre-failure and post-failure remote sensing data to constrain the three-dimensional numerical model of a large rock slope failure. Landslides 18:827–847. https://doi.org/10.1007/s10346-020-01552-x

Donati D, Stead D, Geertsema M, Bendle JM, Menounos B, Borgatti L (2022) Kinematic analysis of the 2020 Elliot Creek landslide, British Columbia, using remote sensing data. Front Earth Sci. https://doi.org/10.3389/feart.2022.916069

Donati D, Stead D, Borgatti L (2023) The importance of rock mass damage in the kinematics of landslides. Geosciences (Basel). https://doi.org/10.3390/geosciences13020052

Esri (2021) ArcGIS 10.9. Available online: www.esri.com (accessed on 15 January 2024)

Fan W, Lv J, Cao Y, Shen M, Deng L, Wei Y (2019) Characteristics and block kinematics of a fault-related landslide in the Qinba Mountains, western China. Eng Geol 249:162–171. https://doi.org/10.1016/j.enggeo.2018.12.019

Firpo G, Salvini R, Francioni M, Ranjith PG (2011) Use of digital terrestrial photogrammetry in rocky slope stability analysis by distinct elements numerical methods. Int J Rock Mech Min Sci 48:1045–1054. https://doi.org/10.1016/j.ijrmms.2011.07.007

Fischer L, Kääb A, Huggel C, Noetzli J (2006) Geology, glacier retreat and permafrost degradation as controlling factors of slope instabilities in a high-mountain rock wall: the Monte Rosa east face. Nat Hazards Earth Syst Sci 6:761–772. https://doi.org/10.5194/nhess-6-761-2006

Fischer L, Purves RS, Huggel C, Noetzli J, Haeberli W (2012) On the influence of topographic, geological and cryospheric factors on rock avalanches and rockfalls in high-mountain areas. Nat Hazards Earth Syst Sci 12:241–254. https://doi.org/10.5194/nhess-12-241-2012

Francioni M, Coggan J, Eyre M, Stead D (2018) A combined field/remote sensing approach for characterizing landslide risk in coastal areas. Int J Appl Earth Obs Geoinf 67:79–95

Francioni M, Salvini R, Stead D, Coggan J (2018b) Improvements in the integration of remote sensing and rock slope modelling. Nat Hazards 90:975–1004. https://doi.org/10.1007/s11069-017-3116-8

Friele P, Millard TH, Mitchell A, Allstadt KE, Menounos B, Geertsema M, Clague JJ (2020) Observations on the May 2019 Joffre Peak landslides. Br Columbia Landslides 17:913–930. https://doi.org/10.1007/s10346-019-01332-2

Froude MJ, Petley DN (2018) Global fatal landslide occurrence from 2004 to 2016. Nat Hazards Earth Syst Sci 18:2161–2181

Geertsema M, Benington A (2020) A cautionary note for rock avalanche field investigation: recent sequential and overlapping landslides in British Columbia. Can Geotech J 58(5):737–740. https://doi.org/10.1139/cgj-2019-0751

Geertsema M, Clague JJ, Schwab JW, Evans SG (2006) An overview of recent large catastrophic landslides in northern British Columbia. Can Geotech J 83:120–143. https://doi.org/10.1016/j.enggeo.2005.06.028

Geertsema M, Menounos B, Bullard G, Carrivick JL, Clague JJ, Dai C, Donati D, Ekstrom G, Jackson JM, Lynett P, Pichierri M, Pon A, Shugar DH, Stead D, Del Bel Belluz J, Friele P, Giesbrecht I, Heathfield D, Millard T, Nasonova S, Schaeffer AJ, Ward BC, Blaney D, Blaney E, Brillon C, Bunn C, Floyd W, Higman B, Hughes KE, McInnes W, Mukherjee K, Sharp MA (2022) The 28 November 2020 landslide, tsunami, and outburst flood – a hazard cascade associated with rapid deglaciation at Elliot Creek, British Columbia, Canada. Geophys Res Lett 49:e2021GL096716. https://doi.org/10.1029/2021GL096716

Gerstner R, Fey C, Kuschel E, Valentin G, Voit K, Zangerl C (2023) Polyphase rock slope failure controlled by pre-existing geological structures and rock bridges. Bull Eng Geol Environ 82:363. https://doi.org/10.1007/s10064-023-03382-2

Goodman RE (1995) Block theory and its application. Geotechnique 45(3):383–423. https://doi.org/10.1680/geot.1995.45.3.383

Grämiger LM, Moore JR, Gischig VS, Ivy-Ochs S, Loew S (2017) Beyond debuttressing: mechanics of paraglacial rock slope damage during repeat glacial cycles. J Geophys Res Earth Surf 122:1004–1036. https://doi.org/10.1002/2016JF003967

Gruber S, Haeberli W (2007) Permafrost in steep bedrock slopes and its temperatures-related destabilization following climate change. J Geophys Res Earth Surf 112:1–10. https://doi.org/10.1029/2006JF000547

Gschwind S, Loew S, Wolter A (2019) Multi-stage structural and kinematicanalysis of a retrogressive rock slope instability complex (Preonzo, Switzerland). Eng Geol 252:27–42

Haeberli W, Wegmann M, Vonder Mühll D (1997) Slope stability problems related to glacier shrinkage and permafrost degradation in the Alps. Eclogae Geol Helv 90(3):407–414. https://doi.org/10.5169/seals-168172

Havaej M, Coggan J, Stead D, Elmo D (2016) A combined remote sensing–numerical modelling approach to the stability analysis of Delabole slate quarry, Cornwall, UK. Rock Mech Rock Eng 49:1227–1245. https://doi.org/10.1007/s00603-015-0805-z

He L, Francioni M, Coggan J, Calamita F, Eyre M (2022) Modelling the influence of geological structures in paleo rock avalanche failures using field and remote sensing data. Remote Sens 14:4090. https://doi.org/10.3390/rs14164090

Hungr O (2007) Dynamics of Rapid Landslides. In: Sassa K, Fukuoka H, Wang F, Wang G (eds) Progress in Landslide Science. Springer, Berlin, Heidelberg. https://doi.org/10.1007/978-3-540-70965-7_4

Hungr O, Leroueil S, Picarelli L (2014) The Varnes classification of landslide types, an update. Landslides 11:167–194. https://doi.org/10.1007/s10346-013-0436-y

ISRM (1978) Suggested methods for the quantitative description of discontinuities in rock masses, in: International Journal of Rock Mechanics and Mining Sciences and Geomechanics Abstracts. pp. 319–368

Itasca (2021a) 3DEC 5.2. Available online: https://www.itascainternational.com/software/3DEC (accessed on 15 January 2024)

Itasca (2021b) Griddle 1.0. Available online: https://www.itascainternational.com/software/Griddle (accessed on 15 January 2024)

Iverson RM (2000) Landslide triggering by rain infiltration. Water Resour Res 36:1897–1910

Jaboyedoff M, Oppikofer T, Abellán A, Derron M-H, Loye A, Metzger R, Pedrazzini A (2012) Use of LIDAR in landslide investigations: a review. Nat Hazards 61:5–28

Jaboyedoff M, Michoud C, Derron MH, Voumard J, Leibundgut G, Sudmeier-Rieux K, Nadim F, Leroi E (2018) Human-induced landslides: toward the analysis of anthropogenic changes of the slope environment. Landslides Eng. Slopes. Exp. Theory Pract. CRC Press, Boca Raton, FL, USA, pp 217–232

Jennings JE (1970) A Mathematical theory for the calculation of the stability of slopes in open cast mines. Proceedings of the Symposium on the Theoretical Background to the Planning of Open Pit Mines with Special References to Slope Stability, 29 August-4 September, Johannesburg, pp. 87–102

Keefer DK (2002) Investigating landslides caused by earthquakes–a historical review. Surv Geophys 23:473–510

Kemeny J (2005) Time-dependent drift degradation due to the progressive failure of rock bridges along discontinuities. Int J Rock Mech Min Sci 42:35–46. https://doi.org/10.1016/j.ijrmms.2004.07.001

Kos A, Amann F, Strozzi T, Delaloye R, von Ruette J, Springman S (2016) Contemporary glacier retreat triggers a rapid landslide response, Great Aletsch Glacier, Switzerland. Geophys Res Lett 43:12–466

Lacroix P, Handwerger AL, Bièvre G (2020) Life and death of slow-moving landslides. Nat Rev Earth Environ 1:404–419. https://doi.org/10.1038/s43017-020-0072-8

Laimer HJ (2017) Anthropogenically induced landslides–a challenge for railway infrastructure in mountainous regions. Eng Geol 222:92–101

Legros F (2002) The mobility of long-runout landslides. Eng Geol 63:301–331

Leinauer J, Weber S, Cicoira A, Beutel J, Krautblatter M (2023) An approach for prospective forecasting of rock slope failure time. Commun Earth Environ 4:253. https://doi.org/10.1038/s43247-023-00909-z

Lemaire E, Dufresne A, Hamdi P et al (2024) Back-analysis of the paraglacial slope failure at Grewingk Glacier and Lake, Alaska. Landslides 21:775–789. https://doi.org/10.1007/s10346-023-02177-6

Loew S, Schneider S, Josuran M et al (2025) Early warning and dynamics of compound rockslides: lessons learnt from the Brienz/Brinzauls 2023 rockslope failure. Landslides 22:283–298. https://doi.org/10.1007/s10346-024-02380-z

Manconi A, Giordan D (2016) Landslide failure forecast in near-real-time. Geomatics Nat Hazards Risk 7:639–648. https://doi.org/10.1080/19475705.2014.942388

Mazzanti P, Bozzano F, Cipriani I, Prestininzi A (2015) New insights into the temporal prediction of landslides by a terrestrial SAR interferometry monitoring case study. Landslides 12:55–68. https://doi.org/10.1007/s10346-014-0469-x

McColl ST (2012) Paraglacial rock-slope stability. Geomorphology 153:1–16. https://doi.org/10.1016/j.geomorph.2012.02.015

McNeel and Associates (2020) Rhinoceros 6. Available online: https://www.rhino3d.com/ (accessed on 15 January 2024)

Michoud C, Jaboyedoff M, Derron M-H, Nadim F, Leroi E (2012) New classification of landslide-inducing anthropogenic activities, in: EGU General Assembly Conference Abstracts. p. 2923

Monger JWH, Gibson HD (2019) Mesozoic-Cenozoic deformation in the Canadian Cordillera: The record of a Continental. Bulldozer? Tectonophysics 757:153–169. https://doi.org/10.1016/j.tecto.2018.12.023

Monger JWH, Price RA, Tempelman-Kluit DJ (1982) Tectonic accretion and the origin of the two major metamorphic and plutonic welts in the Canadian Cordillera. Geology 10:70–75. https://doi.org/10.1130/0091-7613(1982)10%3C;70:TAATOO%3E;2.0.CO;2

Mufundirwa A, Fujii Y, Kodama J (2010) A new practical method for prediction of geomechanical failure-time. Int J Rock Mech Min Sci 47:1079–1090. https://doi.org/10.1016/j.ijrmms.2010.07.001

Perozzo M, Menegoni N, Foletti M, Poggi E et al (2024) Evaluation of an innovative, open-source and quantitative approach for the kinematic analysis of rock slopes based on UAV based Digital Outcrop Model: A case study from a railway tunnel portal (Finale Ligure, Italy). Eng Geol 340:107670. https://doi.org/10.1016/j.enggeo.2024.107670

Roberti G, Ward B, van Wyk de Vries B, Friele P, Perotti L, Clague JJ, Giardino M (2018) Precursory slope distress prior to the 2010 Mount Meager landslide, British Columbia. Landslides 15:637–647. https://doi.org/10.1007/s10346-017-0901-0

RocScience (2024) DIPS 8. Available online: www.rocscience.com (accessed on 4 May 2025)

RocScience (2023) SWedge 7. Available online: www.rocscience.com (accessed on 4 May 2025)

Rose ND, Hungr O (2007) Forecasting potential rock slope failure in open pit mines using the inverse-velocity method. Int J Rock Mech Min Sci 44:308–320. https://doi.org/10.1016/j.ijrmms.2006.07.014

Salvini R, Vanneschi C, Coggan JS, Mastrorocco G (2020) Evaluation of the use of UAV photogrammetry for rock discontinuity roughness characterization. Rock Mech Rock Eng 53:3699–3720. https://doi.org/10.1007/s00603-020-02130-2

Sampaleanu C (2017) The role of intact rock fracture in rockfall initiation, M.Sc. Thesis, Simon Fraser University in British Columbia, Canada

Sartori M, Baillifard F, Jaboyedoff M, Rouiller J-D (2003) Kinematics of the 1991 Randa rockslides (Valais, Switzerland). Nat Hazards Earth Syst Sci 3:423–433. https://doi.org/10.5194/nhess-3-423-2003

Sättele M, Krautblatter M, Bründl M, Straub D (2016) Forecasting rock slope failure: how reliable and effective are warning systems? Landslides 13:737–750. https://doi.org/10.1007/s10346-015-0605-2

Scholtès L, Donzé FV (2012) Modelling progressive failure in fractured rock masses using a 3D discrete element method. Int J Rock Mech Min Sci 52:18–30. https://doi.org/10.1016/j.ijrmms.2012.02.009

Sepúlveda SA, Tobar C, Rosales V, Ochoa-Cornejo F, Lara M (2023) Megalandslides and deglaciation: modelling of two case studies in the Central Andes. Nat Hazards 118(2):1561–1572. https://doi.org/10.1007/s11069-023-06067-x

Spreafico MC, Francioni M, Cervi F, Stead D, Bitelli G, Ghirotti M, Girelli VA, Lucente CC, Tini MA, Borgatti L (2016) Back analysis of the 2014 San Leo landslide using combined terrestrial laser scanning and 3D distinct element modelling. Rock Mech Rock Eng 49:2235–2251. https://doi.org/10.1007/s00603-015-0763-5

Stead D, Eberhardt E (2013) Understanding the mechanics of large landslides. Ital J Eng Geol Environ 2013:85–119. https://doi.org/10.4408/IJEGE.2013-06.B-07

Stead D, Wolter A (2015) A critical review of rock slope failure mechanisms: the importance of structural geology. J Struct Geol 74:1–23. https://doi.org/10.1016/j.jsg.2015.02.002

Stead D, Donati D, Wolter A, Sturzenegger M (2019) Application of remote sensing to the investigation of rock slopes: experience gained and lessons learned. ISPRS Int J Geo-Inf. https://doi.org/10.3390/ijgi8070296

Steffen OKH (1978) Some aspects of three dimensional and two dimensional rock slopes stability analysis with two case histories, PhD, Thesis, University of Witwatersrand, South Africa

Sturzenegger M, Stead D, Gosse J, Ward B, Froese C (2015) Reconstruction of the history of the Palliser Rockslide based on 36Cl terrestrial cosmogenic nuclide dating and debris volume estimations. Landslides 12:1097–1106. https://doi.org/10.1007/s10346-014-0527-4

Terzaghi K (1962) Stability of steep slopes on hard unweathered rock. Géotechnique. https://doi.org/10.1680/geot.1962.12.4.251

Vandall TA (1993) Cretaceous Coast Belt paleomagnetic data from the Spetch Creek pluton, British Columbia: evidence for the tilt and moderate displacement model. Can J Earth Sci 30:1037–1048. https://doi.org/10.1139/e93-087

Vanneschi C, Eyre M, Francioni M, Coggan J (2017) The use of remote sensing techniques for monitoring and characterization of slope instability. Procedia Eng. https://doi.org/10.1016/j.proeng.2017.05.166

Westoby MJ, Brasington J, Glasser NF, Hambrey MJ, Reynolds JM (2012) Structure-from-motion photogrammetry: a low-cost, effective tool for geoscience applications. Geomorphology 179:300–314. https://doi.org/10.1016/j.geomorph.2012.08.021

Willenberg H, Loew S, Eberhardt E, Evans KF, Spillmann T, Heincke B, Maurer H, Green AG (2008) Internal structure and deformation of an unstable crystalline rock mass above Randa (Switzerland): Part I — internal structure from integrated geological and geophysical investigations. Eng Geol 101:1–14. https://doi.org/10.1016/j.enggeo.2008.01.015

Publisher's note Springer Nature remains neutral with regard to jurisdictional claims in published maps and institutional affiliations.